Managing radiation degradation of CCDs on the Chandra X-ray Observatory—II

Stephen L. O'Dell[*a], Thomas L. Aldcroft[b], Bradley A. Bissell[c], William C. Blackwell[d], Robert A. Cameron[†b], Jon H. Chappell[b], Joseph M. DePasquale[b], Kenneth R. Gage[c], Catherine E. Grant[e], Christine F. Harbison[c], Michael Juda[b], Kevin A. Marsh[c], Eric R. Martin[c], Joseph I. Minow[f], Stephen S. Murray[b], Paul P. Plucinsky[b], Daniel A. Schwartz[b], Daniel P. Shropshire[c], Bradley J. Spitzbart[b], Shanil N. Virani[‡b], Brent S. Williams[c], and Scott J. Wolk[b]

[a] NASA Marshall Space Flight Center, NSSTC/XD12, 320 Sparkman Dr., Huntsville, AL 35805
[b] Harvard–Smithsonian Center for Astrophysics, 60 Garden St., Cambridge, MA 02138
[c] Northrop Grumman Space Technology, CfA/MS33, 60 Garden St., Cambridge, MA 02138
[d] Jacobs Sverdrup, Sverdrup/MSFC, P.O. Box 9030, Huntsville, AL 35812
[e] MIT Kavli Institute for Astrophysics and Space Research, 77 Massachusetts Ave., Cambridge, MA 02139
[f] NASA Marshall Space Flight Center, MSFC/EV13, Huntsville, AL 35812

ABSTRACT

The CCDs on the Chandra X-ray Observatory are vulnerable to radiation damage from low-energy protons scattered off the telescope's mirrors onto the focal plane. Following unexpected damage incurred early in the mission, the Chandra team developed, implemented, and maintains a radiation-protection program. This program—involving scheduled radiation safing during radiation-belt passes, intervention based upon real-time space-weather conditions and radiation-environment modeling, and on-board radiation monitoring with autonomous radiation safing—has successfully managed the radiation damage to the CCDs. Since implementing the program, the charge-transfer inefficiency (CTI) has increased at an average annual rate of only 3.2×10^{-6} (2.3%) for the front-illuminated CCDs and 1.0×10^{-6} (6.7%) for the back-illuminated CCDs. This paper describes the current status of the Chandra radiation-management program, emphasizing enhancements implemented since the original paper.

Keywords: X-ray astronomy, CCDs, radiation damage, radiation environment, spacecraft operations

1. INTRODUCTION

Now 6 years into its mission, the *Chandra X-ray Observatory*[1, 2, 3] continues to provide superb arcsecond imaging, imaging spectrometry, and high-resolution dispersive spectroscopy. *Chandra*'s Science Instrument Module (SIM) houses 2 instruments, each with an imaging (I) array and with a spectroscopy (S) array for reading spectra dispersed by transmission gratings. The High-Resolution Camera[4] (HRC) uses microchannel plates. The Advanced CCD Imaging Spectrometer[5] (ACIS) has 10 CCDs: ACIS-I comprises a 2×2 CCD array; ACIS-S, a 6×1 CCD array. Of the 10 CCDs, 2 CCDs—both in the S array—are back-illuminated (BI); the remaining 8 CCDs are front-illuminated (FI).

Upon initial *Chandra* operations, the ACIS FI CCDs experienced rapid degradation[6]—a significant increase in charge-transfer inefficiency (CTI). While the CTI of FI CCDs increased, the CTI of BI CCDs did not; nor did the dark current of either device increase: These symptoms indicate that weakly penetrating, low-energy (0.1–0.5-MeV) protons caused this damage.[7] An urgent anomaly investigation concluded that trapped protons[8] had Rutherford scattered off *Chandra*'s x-ray mirrors[9] onto the CCDs during the 8 radiation-belt passages that ACIS had been in the focal position.

[*] Contact author: Steve.O'Dell@nasa.gov; phone 1 256-961-7776; fax 1 256-961-7213; wwwastro.msfc.nasa.gov
[†] Current address: Stanford Linear Accelerator Center, SLAC MS-43A, 2575 Sand Hill Road, Menlo Park, CA 04767
[‡] Current address: Astronomy Department, Yale University, P.O. Box 20810, New Haven, CT 06520

Fortunately, upon recognition of this unforeseen problem, the *Chandra* team immediately modified operating procedures to ensure that the ACIS never remained in the focal position during radiation-belt passes. This policy soon became the keystone to a radiation-protection program[10] (Paper I) that has successfully limited subsequent radiation damage to acceptable levels. Here we report the status (§2) of that program and describe recent enhancements (§3).

2. STATUS

Here we discuss *Chandra*'s orbit and radiation environment (§2.1) and the *Chandra* radiation-protection program (§2.2). With this program in place, increases in the CTI of ACIS CCDs have remained within budgeted levels (§2.3).

2.1. Orbit and radiation environment

The *Chandra X-ray Observatory* is in a highly elliptical orbit, with a 63.5-h period and 80.8-Mm (12.7-$R_\oplus$) semi-major axis. In the 6 years since reaching operational orbit, *Chandra*'s orbital eccentricity and inclination have evolved from 0.800 and 28.5° to 0.563 and 57.5°, respectively. Therefore, *Chandra*'s apogee and perigee altitudes have changed from 139 Mm and 10 Mm (22.8 $R_\oplus$ and 2.5 $R_\oplus$, geocentric) to 120 Mm and 29 Mm (19.8 $R_\oplus$ and 5.5 $R_\oplus$, geocentric), respectively. Figure 1 (left) shows the evolution of the orbit's inclination, apogee, and perigee, over 15 years.

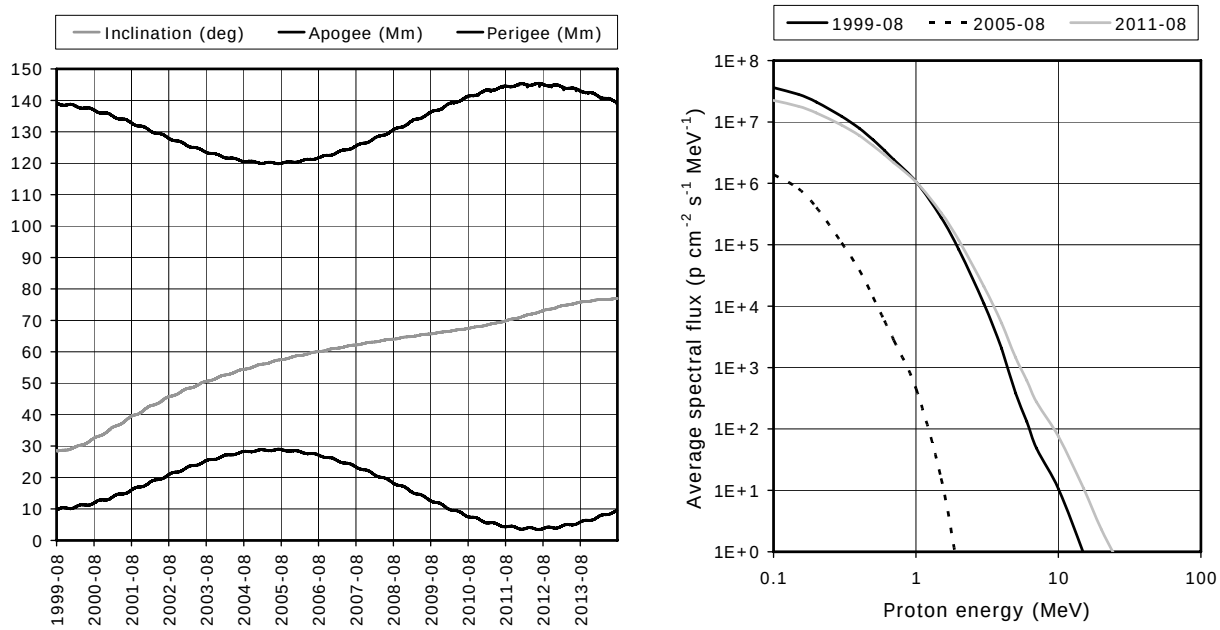

Figure 1: Evolution of *Chandra*'s orbit and external exposure to trapped protons. Left panel exhibits the orbit's apogee and perigee (black lines) and inclination (gray line), from 1999 August (first light) to 2014 August. Right panel illustrates the dependence upon orbit of the average spectral intensity of trapped protons: The black solid line denotes value at first light (1999); black dashed line, 6 years later (2005); and gray solid line, another 6 years later (2011).

As Figure 1 (left) illustrates, the perigee of *Chandra*'s orbit varies about its mean value (≈ 16 Mm) quasi-sinusoidally with approximately a 13-y period and 13-Mm amplitude. Currently, at 6 years into the mission, the perigee is near a maximum. Consequently, *Chandra*'s exposure to the Earth's radiation belts is substantially less at this time than at the start of the mission; but it will now increase. Figure 1 (right) shows the orbit-averaged trapped-proton spectrum, obtained using the SPace ENVironment Information System[11] (SPENVIS) tool to propagate *Chandra*'s orbit through the standard AP8 radiation environment. If ACIS were left in focal position during perigee passes, the rate of radiation damage due to low-energy (0.1–0.5 MeV) trapped protons would be about 2 orders of magnitude less now than during initial operations, but it would be comparable to the initial rate in another 6 years. Of course, this observation is moot: ACIS will never again be exposed to trapped protons during a perigee pass. Indeed, the command load always instructs the SIM translation table to remove the ACIS from focal position by about 70-Mm altitude (12 $R_\oplus$ geocentric).

2.2. Radiation-protection program

The obvious radiation-protection strategy is to limit exposure of the ACIS to high proton-flux environments. In order to accomplish this, the radiation-protection program (Paper I[10]) employs scheduled (§2.2.1), manual (§2.2.2), and autonomous (§2.2.3) radiation safing. In each case, radiation-safing actions are the same—stop science observations, translate ACIS into next-in-line (NIL) position, power down ACIS video boards, and ramp down HRC high voltage.

2.2.1. Scheduled protection

Nominally once a week, the *Chandra* Operations Control Center (OCC) at the *Chandra* X-ray Center (CXC) transmits through NASA's Deep-Space Network (DSN) a command load for *Chandra*'s on-board computer (OBC) to execute autonomously all science observations and other scheduled operations. Prior to radiation-zone ingress, each load explicitly safes the ACIS and HRC against radiation damage; after egress, the command load resumes science observations. In order to set the time to protect the science instruments and the time to resume science observations, the mission planners utilize the standard AP8/AE8 environment, with AE8 being the more restrictive. Because these models are not perfect and because the radiation zones—especially the outer electron zone—exhibit substantial transient and localized variations, it is necessary to pad the AE8-predicted times by a few hours. Recently, the science operations team completed a study and implemented changes to optimize these radiation-zone pad times (§3.1).

Scheduled protection prevents the rapid increase in FI-CCD CTI suffered during proton-belt transits. However, transient events elsewhere in the radiation environment—solar radiation storms, solar-wind shocks, and geomagnetic storms—contain proton fluences that would noticeably degrade CCD performance over time. Thus, the *Chandra* team developed and implemented additional steps (§2.2.2 and §2.2.3) to limit exposure of the ACIS to such events.

2.2.2. Manual intervention

Chandra has an on-board radiation monitor that the OBC uses autonomously (§2.2.3) to protect the science instruments against certain severe radiation events—such as inadvertent, unprotected radiation-belt entry. However, the radiation-monitor data (like all *Chandra* data) are available in real time or via data dump only during DSN contacts, typically for about an hour every 8 hours or so. Furthermore, the *Chandra* radiation monitor is not sensitive to the low-energy protons responsible for damaging the ACIS CCDs. For these reasons, the team implemented an extensive monitoring program using real-time environments data from other spacecraft, available through the National Oceanographic and Atmospheric Administration (NOAA) Space Environment Center (SEC).

The *GOES* proton monitor and the *Advanced Composition Explorer*[12] (*ACE*) Solar Isotope Spectrometer[13] (SIS) transmit real-time data for protons more energetic than 5 MeV and 10 MeV, respectively. *GOES* satellites are in geostationary orbits, while *ACE* is near the first Lagrange (L1) point. In order to get real-time data at altitudes more representative of *Chandra*'s orbit, the science operations team recently arranged (§3.2) to retrieve near-real-time data from the radiation monitor aboard ESA's XMM-*Newton*. Because solar protons more energetic than about 5 MeV typically penetrate the Earth's magnetosphere down to geosynchronous orbit, the *GOES* proton monitor serves as an effective real-time predictor between DSN contacts, of the count rate in the corresponding proton channels of *Chandra*'s on-board radiation monitor (§2.2.3).

The *ACE* Electron, Proton, and Alpha Monitor[14] (EPAM) provides the most relevant data—namely, the low-energy (0.05–2-MeV) proton spectrum in the solar wind. To supplement the *ACE* EPAM data, MSFC's space environments group developed the *Chandra* Radiation Model[15] (CRM). Used in conjunction with *ACE* data, the CRM permits real-time estimation of the 0.14-MeV-proton spectral intensity throughout *Chandra*'s orbit, which passes through 3 space-environment regions—(1) solar wind, (2) magnetosheath, and (3) magnetosphere. Recently, the space environments group updated (§3.3) the CRM.

The *Chandra* team carefully monitors the 0.14-MeV-proton orbital fluence measured by the *ACE* EPAM (in the solar wind) and estimated by the real-time CRM, and issues an alert (via pager and e-mail) if the 2-hour fluence exceeds a specified value. Based upon this or other automated alerts or upon concerns of personnel watching the radiation environment, the team convenes via teleconference, evaluates the radiation environment, and decides whether to intervene manually upon the next scheduled DSN contact, by activating the radiation-protection stored command sequence (SCS107). The team re-convenes as needed until the radiation threat has passed, the mission planners have built a new load, and science observations have resumed. Through the first 6 years of the mission, the team manually protected the science instruments 20 times for 1.9-Ms lost science.

2.2.3. Autonomous protection

The Electron, Proton, Helium Instrument[16] (EPHIN, §3.5.1)—flight spare for the *SOlar & Heliospheric Observatory* (*SOHO*)—serves as *Chandra*'s on-board radiation monitor. EPHIN collects data in 4 electron channels (0.25–10.4 MeV), 4 proton channels (4.3–53 MeV), 4 helium channels (4.3–53 MeV/n), and an integral channel. During DSN contacts, *Chandra* downloads all EPHIN data for CXC use and for space-physics science by the EPHIN science team.

During normal *Chandra* operations, the process "RADMON" runs on the OBC, sampling and evaluating 3 EPHIN channels—P4 (4.3–7.8-MeV proton), P41 (41–53-MeV proton), and E1300 (2.6–6.2-MeV electron)—that serve as the real-time radiation monitor. If the count rate in any of these 3 channels exceeds its respective pre-set threshold for N consecutive 65.6-s samples, the OBC autonomously activates the radiation-protection stored command sequence (SCS107). Recently, the *Chandra* team increased the number N—from 3 to 10—of over-threshold samples required to activate SCS107, in order to reduce spurious or otherwise unnecessary triggers (§3.4).

Through its first 6 years, *Chandra* autonomously protected the science instruments 37 times for 4.1-Ms lost science. Most SCS107 triggers resulted from solar-energetic-particle (SEP) events accompanying major solar flares: This is the type of hard-proton event for which the radiation monitor was originally intended. Several SCS107 triggers occurred just prior to scheduled protection (§2.2.1) for radiation-zone ingress: These events resulted from electron-flux spikes (§3.4) that present no danger to the science instruments. A few SCS107 triggers happened immediately following re-enabling of the RADMON process following a radiation safing: In these cases, a single above-threshold sample (either real or stale data) triggered SCS107 before the above-threshold counter had cleared from the previous radiation event.

Due to elevated EPHIN temperatures resulting from degradation of its multi-layer insulation (MLI), the data in some EPHIN channels may eventually become noisy. In order to prepare for this possibility, the CXC and HRC teams recently prepared contingency plans for using the HRC anti-coincidence shield as a radiation monitor (§3.5).

2.3. Charge-transfer inefficiency

The radiation-protection program (§2.2) has successfully reduced the rate of CTI increase to manageable levels. Figure 2 displays the CTI since 2000 January, after cooling the ACIS focal plane to its current operating temperature (-120°C). Displayed CTI measurements[17] are from the ACIS (Fe^{55}) external calibration source (ECS), which ACIS views while stowed in the NIL position, and are corrected for sacrificial charge[18] from cosmic rays. Currently, the FI-CCD CTI = 16.0×10^{-5}; the BI-CCD CTI = 2.0×10^{-5}. Since 2001 January, the CTI has increased at 0.29×10^{-5} /y (1.8%/y) for FI CCDs and at 0.08×10^{-5} /y (4.2%/y) for BI CCDs—slightly less than the average rates since 2000 January. Hence, the rate of CTI increase is sufficiently small to allow ACIS to continue to provide spectrometric imaging for decades.

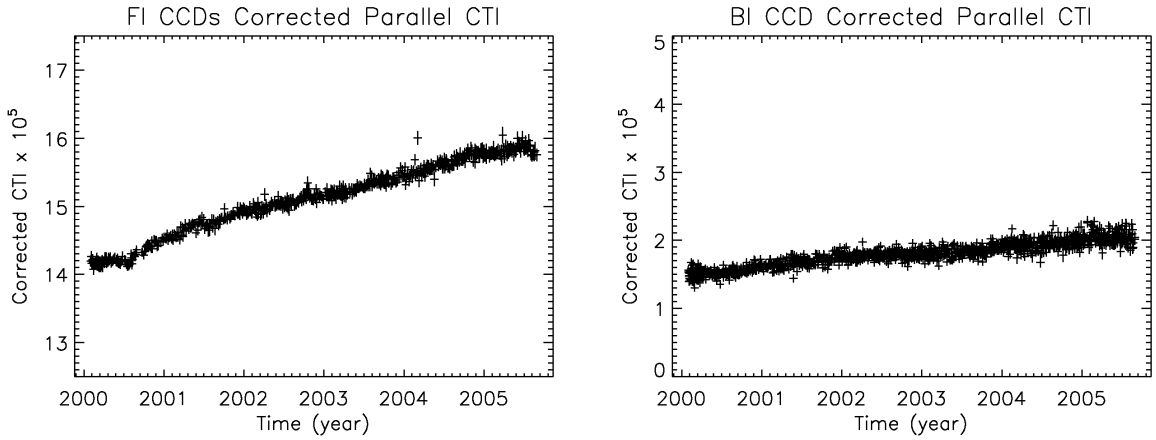

Figure 2: Charge transfer inefficiency (CTI) of ACIS CCDs at 5.9 keV (Mn–Kα), for the focal plane at -120°C, corrected for cosmic-ray sacrificial charge. Left panel shows the average CTI of the 4 front-illuminated CCDs comprising the imaging (I) array; right panel, the CTI of the back-illuminated CCD (S3) at the center of the spectroscopy (S) array.

CXC data processing now implements a CTI corrector, originally developed by the ACIS team.[19, 20] The CTI corrector removes the non-stochastic part of the CTI-induced position-dependent gain error. Thus, the FI CCDs continue to

provide high-resolution imaging spectrometry[21]—albeit with poorer energy resolution than originally expected. The CTI of the BI devices is an order of magnitude less than that of the radiation-damaged FI CCDs, but currently increasing at about 0.3 the rate of that of the FI CCDs. In contrast, the unprotected radiation-belt passes, which produced the initial damage in the FI devices, resulted in no measurable increase in the CTI of the BI CCDs. This indicates[17] that the average spectrum of protons reaching the ACIS CCDs is now significantly harder than during the unprotected radiation-belt passes. Note that 1.9×10^{-4} g cm^{-2} shields the FI charge transfer channel from protons under 0.1 MeV; 1.2×10^{-2} g cm^{-2} (45-μm silicon) shields the BI charge transfer channel from protons under 2.2 MeV.

3. ENHANCEMENTS

We introduced several enhancements to the radiation-protection program (§2.2) since Paper I.[10] For scheduled protection (§2.2.1), we reduced pad times on AE8 predictions of radiation-zone ingress and egress so as to increase science time (§3.1). For manual intervention (§2.2.1), we added access to real-time data from the XMM-*Newton* radiation monitor (§3.2); we updated the Chandra Radiation Model (CRM) to include data through 2004 that more fully populates relevant parameter space (§3.3). For autonomous protection (§2.2.3), we increased the number of EPHIN samples required to activate radiation safing, in order to reduce unnecessary triggers (§3.4); we developed contingency procedures to use the HRC anti-coincidence shield as a radiation monitor if EPHIN data become problematic (§3.5).

3.1. Radiation-zone pad times

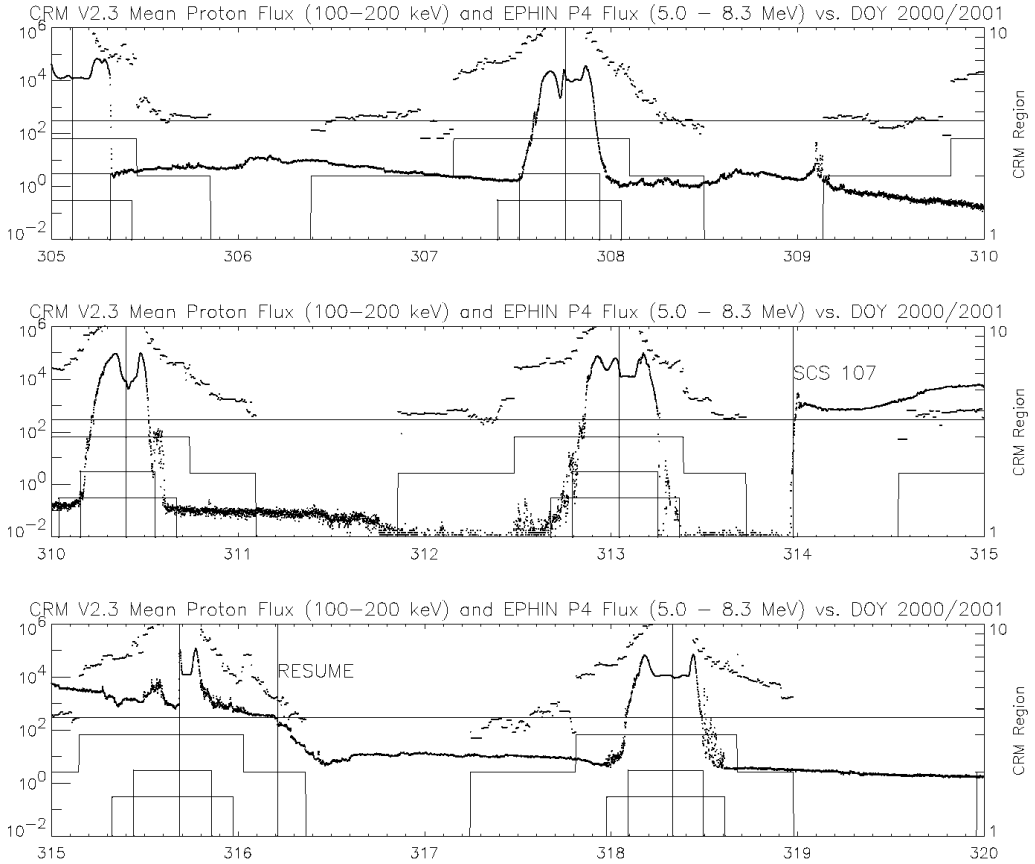

Figure 3: EPHIN P4 and mean-CRM proton intensity from 2000 Oct. 31 to Nov. 15. Intensity units on the primary ordinate are p/(cm^2 s sr) for EPHIN but p/(cm^2 s sr MeV) for CRM. The secondary ordinate indicates the CRM region—(1) solar wind, (2) magnetosheath, and (3) magnetosphere. Horizontal lines give the P4 SCS107 threshold, duration of RADMON disable, and duration of E1 (electron-zone) transit. Note the autonomous SCS107 near the start of day 314.

Early in the mission, the science operations and EPHIN teams had compared[22] *Chandra* EPHIN data with AE8/AP8 predictions of radiation-zone ingress and egress (cf. Figure 3). This study showed that the more restrictive AE8 predictions were not sufficiently accurate, primarily due to temporal variations in the outer electron zone. To preclude excessive autonomous radiation safing (§2.2.3), mission planners applied a 10-ks pad to the AE8-predicted electron zone (E1). Subsequent analyses[23, 24] of combined mean-CRM and EPHIN data sets from 1999 November to 2003 February, found a 10-ks pad on E1 to be overly conservative: Use of a CRM-predicted variable pad time could have regained 1.4-Ms observing time over that period. Consequently, in 2004 March, mission planners began using the variable CRM-predicted pad times, which recovered approximately 0.2-Ms observing time in its first year of use.

3.2. XMM-*Newton* radiation monitor

In mid-2004, The XMM-*Newton* program made available near-real-time data from its on-board EPIC (European Photon Imaging Camera) radiation monitor[25] (ERM). The ERM comprises 2 detectors: The Low-Energy (LE) unit detects 0.13–1.5-MeV electrons and 1.0–4.5-MeV protons; the High-Energy (HE) unit, 0.5–2.5-MeV electrons and 12.5–100-MeV protons. For each unit, counters provide count rates for specific energy bands and integrated over energy. The XMM-*Newton* Science Operations Centre (Vilspa) pushes near-real-time ERM data to the CXC every 5 minutes, which the CXC data system processes with a latency of about 10 minutes. Figure 4 displays a CXC plot of ERM near-real-time data supplemented by ancillary information—altitude and radiation-environment region—on spacecraft location.

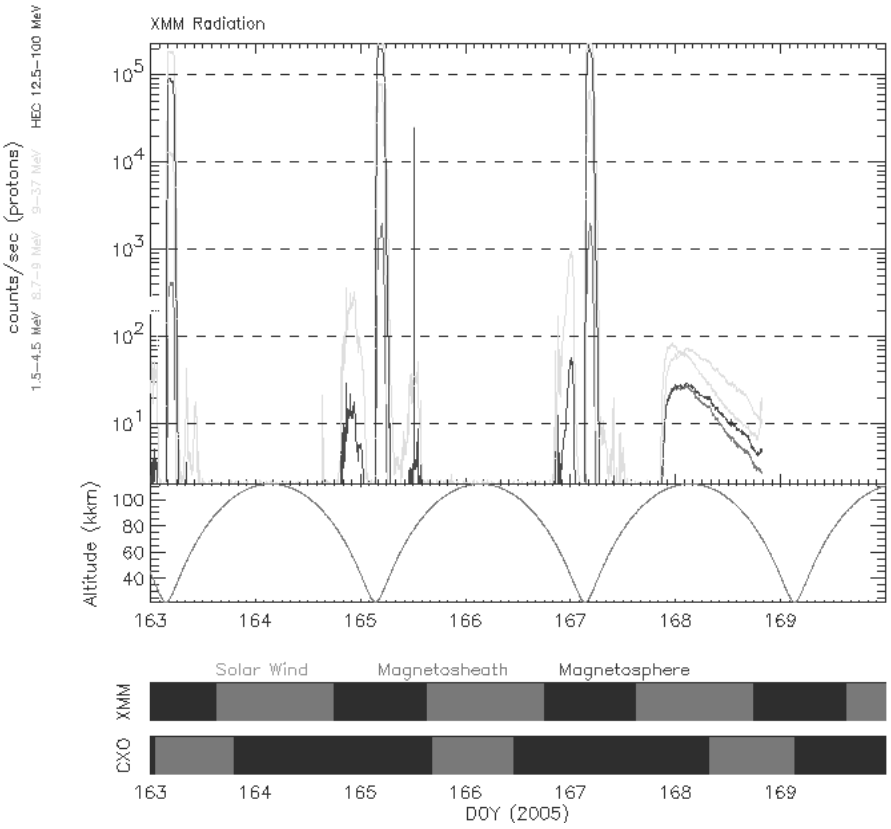

Figure 4: Plot of data from the XMM-*Newton* EPIC radiation monitor detector (ERM), for a 7-d (3.5-orbit) sample of the near-real-time data. Top panel displays rates for 5 of 7 ERM counters; middle panel, spacecraft altitude; and bottom panel, radiation region (solar wind, magnetosheath, or magnetosphere) of XMM-*Newton* and *Chandra* orbital locations.

In that 0.1–0.5-MeV protons caused most of the initial damage to the ACIS FI CCDs, the CXC monitors most closely the ERM lowest-energy counter (LE1) for the 1.0–1.5-MeV-proton band. If the LE1 count rate exceeds a specified threshold, the CXC can issue an alert (via e-mail and pager). Note that the energy band of the ERM LE1 is similar to that of the *ACE* EPAM[14] highest energy (1.1–1.9-MeV) proton band (P7), which the CXC tracks in near real time along

with other *ACE* data (§2.2.2). However, whereas *ACE* is at L1, XMM-*Newton* is in a highly elliptical orbit (48.0-h period, 66.9-Mm semi-major axis) similar to that of *Chandra*. Thus, to the extent geomagnetic effects affect 1-MeV protons, the ERM-measured values are more indicative of the radiation environment to which *Chandra* is exposed.

3.3. Chandra radiation model

The Chandra Radiation Model[15] (CRM) is a 3-dimensional map of the 0.14-MeV-proton spectral intensity (Figure 5). We derive the CRM from a correlation of archival data—from the *Geotail* Energetic Proton and Ion Composition (EPIC) detector[26] and from the *Polar* Comprehensive Energetic-Particle Pitch Angle Distribution (CEPPAD) instrument[27]—with the geomagnetic planetary index Kp. In order to populate fully the data cube throughout the domain of geocentric radii 8–32 $R_\oplus$, we also map the particle distribution along the magnetic field—"field-line mapping". Recently, we updated the CRM to include *Geotail* EPIC and *Polar* CEPPAD data through 2004, which significantly increased data coverage for high-Kp periods. Figure 5 exhibits an equatorial slice in Geocentric Solar Magnetospheric (GSM) coordinates, of the updated CRM data cube for geomagnetic conditions characterized by Kp = 1 (quiet), 3 (moderate), 5 (minor storm), and 7 (strong storm). Note the three distinct radiation regions—(1) solar wind, (2) magnetopause, and (3) magnetosphere—separated by the bow shock and by the magnetopause, respectively.

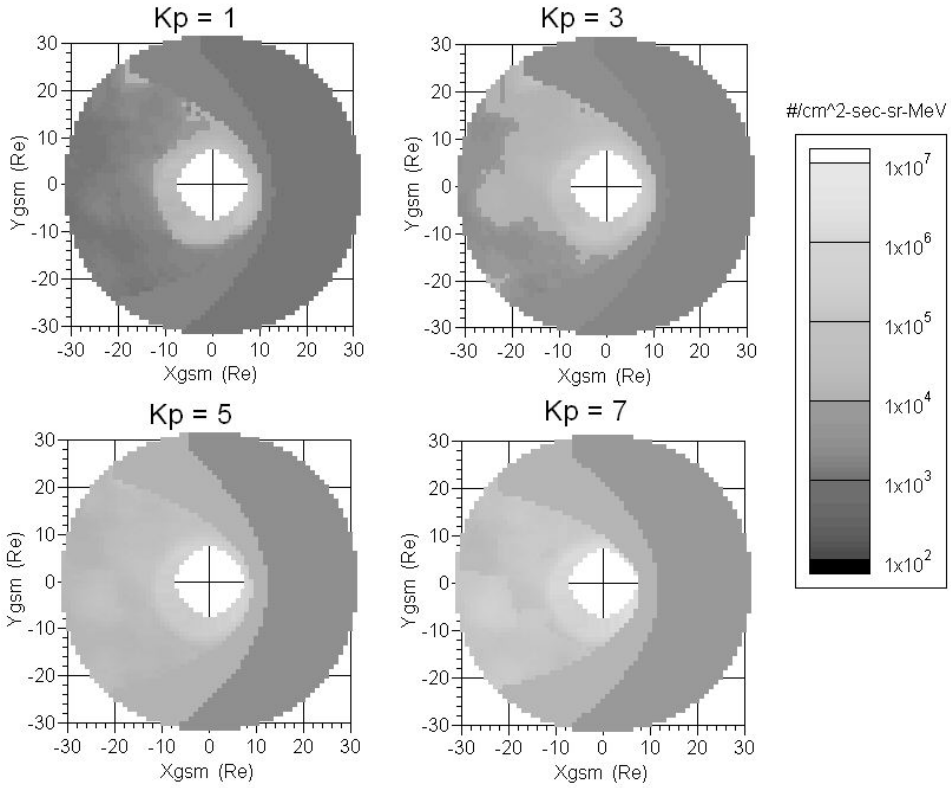

Figure 5: Chandra Radiation Model (CRM) for 0.14-MeV protons at geocentric distances 8–32 $R_\oplus$ for 4 values of the geomagnetic planetary index Kp. Each displayed map is an equatorial slice in geocentric solar magnetospheric (GSM) coordinates, with the sun on the $+X_{gsm}$ axis and the Earth's magnetic poles in the X_{gsm}–Z_{gsm} plane.

We employ the CRM for multiple purposes. Mission planners now schedule radiation protection for perigee passes using radiation-zone pad times (§3.1) derived from a combined analysis[23, 24] of archival EPHIN and mean-CRM data. For real-time estimation, *ACE* Solar-Wind Electron Proton Alpha Monitor[28] (SWEPAM) data[29] drives the SEC-provided (neural-net) Costello Kp estimator[30], which in turn drives our Kp-dependent CRM estimator of proton intensity. This allows a real-time estimate of 0.14-MeV-proton fluence from the start of an orbit. For an assumed value of Kp, we can also project the fluence for the rest of that orbit. If the estimated fluence exceeds a budgeted amount, we can decide whether to intervene (§2.2.2) by manually activating radiation safing (SCS107) at the next DSN contact.

Naturally, the *ACE* EPAM P3 channel furnishes the best real-time estimator for the 0.14-MeV-proton spectral intensity when *Chandra* is in the solar wind. In the magnetosheath (between bow shock and magnetopause), the population may have contributions from shocked solar-wind protons and from protons leaking from the magnetosphere. In the magnetosphere, the population may have contributions from quasi-trapped magnetospheric protons and from solar-wind protons penetrating the magnetopause. Thus, we adopt a conservative approach and utilize a hybrid of real-time EPAM data and the real-time SWEPAM-Kp–driven CRM estimate:

1. Solar wind $F_1(t) = F_{EPAM}(t)$
2. Magnetosheath $F_2(t) = 2 \times F_{EPAM}(t) + F_{CRM}(Kp(t))$
3. Magnetosphere $F_3(t) = F_{CRM}(Kp(t)) + \frac{1}{2} \times F_{EPAM}(t)$

3.4. Electron spikes

For most perigee passes, scheduled radiation protection (2.2.1)—based upon padded times (§3.1) for AE8-predicted radiation-zone (E1) ingress and egress—proceeds normally: The command load stops science observations, stows ACIS in NIL position, and then resumes science operations after leaving the outer radiation zone. However, large transient increases in EPHIN (§2.2.3) count rates outside the predicted outer electron zone have occasionally triggered autonomous activation of radiation safing (SCS107) prior to scheduled protection. These events are disruptive in that they unnecessarily halt science observations and may leave the spacecraft in an undesirable state—e.g., at a bad attitude for thermal control. Thanks to the mission planners, who have invariably re-built the load in time to resume science operations upon radiation-zone egress, these events generally result in little lost time for science observations.

Although the flux spikes result in EPHIN count rates that exceed threshold in either the P4 (4.3–7.8-MeV proton) or the E1300 (2.6–6.2-MeV electron) channel, the (University of Kiel) EPHIN team has shown that the high P4 rates actually result from contamination by a very high flux of electrons. Hence, these events do not produce displacement damage in the ACIS CCDs; nor are they sufficiently intense to produce coronal discharge in the HRC high-voltage electronics. Therefore, the *Chandra* team determined that these electron-flux events present no risk. Furthermore, the frequency of these events was increasing to the point that these unnecessary safings were a nuisance and a drain on resources. Hence, we developed a strategy for ignoring these benign events without risking damage from true proton events.

After considering several strategies, we adopted a simple modification to the RADMON process that safely eliminated nearly all SCS107 triggers from electron spikes. The key is time: RADMON watches flux; ACIS damage results from fluence (dose). Even a very large flux of protons produces little radiation damage to CCDs if the exposure is sufficiently short. Studies by the MSFC environments group and by the (CXC) science operations team showed nearly all electron spikes are above RADMON thresholds for less than an hour. However, ACIS CCDs can tolerate the largest proton flux credible outside the trapped-proton belt, for a few hours without detectible CTI increase. Consequently, we increased from 3 to 10 the number of over-threshold 65.6-s EPHIN samples required to trigger SCS107.

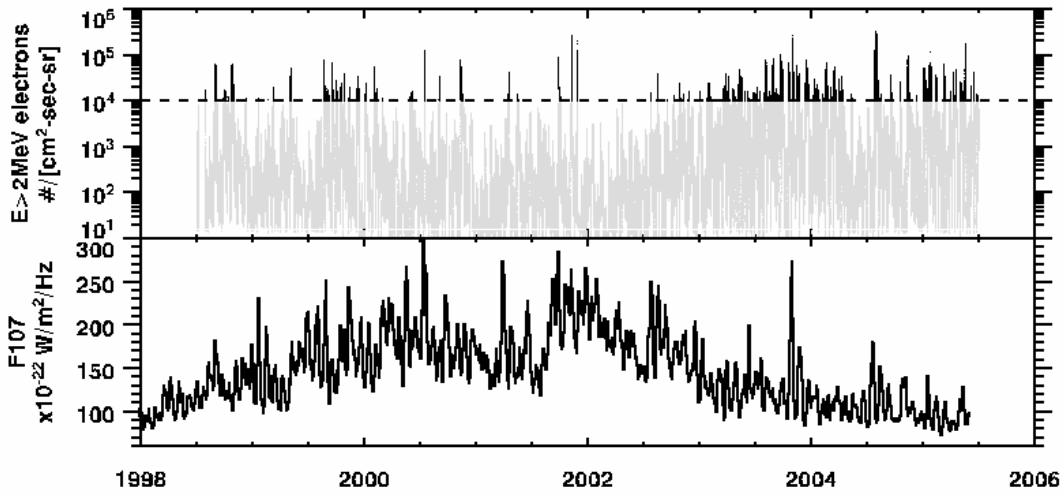

Figure 6: Frequency of electron-flux spikes relative to solar activity. Top panel gives >2-MeV-electron intensity at (GOES-10) geostationary orbit; bottom panel, the solar 10.7-cm radio flux density—a proxy index of solar activity.

Since the start of the mission, electron spikes had become more frequent just before entering the outer electron zone. This occurred as *Chandra*'s orbit evolved toward higher inclination and smaller eccentricity. *Chandra* now spends more time at higher magnetic latitudes, the magnetosphere's most variable electron environment. Also, the solar cycle transitioned from maximum toward minimum. During the solar-cycle declining phase, recurrent high-speed streams from coronal holes are more prevalent: These streams are particularly efficient at enhancing relativistic-electron fluxes in the magnetosphere.[31, 32, 33] Figure 6 (top) shows the intensity of >2-MeV electrons at 1-min resolution, measured in geostationary orbit. As this plot illustrates, large electron spikes were rare during 2000–2002 but became more frequent during 2003–present. Figure 6 (bottom, from NOAA's National Geophysical Data Center) shows that the solar 10.7-cm radio flux density (F10.7), a proxy index of solar activity, is relatively low during periods of frequent electron spikes.

3.5. EPHIN thermal degradation

During the mission, the thermal-control properties of *Chandra*'s silverized-Teflon multilayer insulation (MLI) have degraded, probably due to radiation damage during perigee passes and thermo-mechanical stresses during sun-angle changes. While thermal control of the Observatory itself has adequate margin, that of the Electron, Proton, Helium Instrument (EPHIN) does not. Designed to monitor solar energetic particles, EPHIN resides on the sunward side of the spacecraft, unshaded during normal operations. Temperatures experienced by EPHIN detectors and electronics will continue to rise as the MLI's solar absorptance further increases. Limiting sun angles to minimize near-normal illumination of EPHIN helps; however, this practice constrains mission planning and will eventually be insufficient. Thus, we expect that progressively higher temperatures will eventually degrade EPHIN's performance and efficacy as a radiation monitor. Here we consider (§3.5.1) the anticipated impact of rising EPHIN temperatures, describe (§3.5.2) potential use of the HRC anti-coincidence shield as a radiation monitor, compare (§3.5.3) HRC anti-co rates and EPHIN rates; and discuss (§3.5.4) contingency plans to replace EPHIN data used by RADMON (§2.2.3) with HRC anti-co data.

3.5.1. Potential impacts

The EPHIN instrument[16] uses coincidences in a stack of 6 detectors—3 ion-implanted Si detectors ("A", "B", and "F") and 3 lithium-drifted Si [Si(Li)] detectors ("C", "D", and "E")—plus a guard detector ("G", a scintillator read by a photomultiplier tube, PMT), to assign the species and energy of incident particles. The EPHIN Input/Output (EIO) interfaces between EPHIN and the spacecraft and collects EPHIN data—including counts in a number of coincidence channels corresponding to various particle energy ranges—for inclusion in telemetry. Currently, the OBC RADMON process watches 3 of 13 EPHIN coincidence channels—E1300, P4, and P41 (§2.2.3).

The EPHIN team anticipates that elevated temperatures will eventually degrade performance of the Si(Li) detectors through more rapid Li diffusion. Further, elevated temperatures have raised the detectors' leakage currents, triggering episodes of reduced high voltage: This also would increase the Li diffusion rate if the bias drops too low. The expected degradation symptom is increased noise in the Si(Li) detectors. This may ultimately render detectors C, D, and E unusable, thus making EPHIN channels using those detectors—i.e., the higher energy channels—problematic. However, there are steps to mitigate the adverse impact of increased Si(Li)-detector noise upon the radiation-protection program—e.g., adjusting RADMON trigger levels, averaging samples, or watching alternate EPHIN channels.

3.5.2. HRC anti-coincidence shield

The HRC[4] anti-coincidence ("anti-co") shield comprises plastic scintillator blocks that surround the detector housing on 5 sides, read by 1 of 2 photomultiplier tubes (PMTs). The purpose of the anti-co shield is to detect charged particles that penetrate the microchannel-plate (MCP) detectors, in order to distinguish (through coincidence) charged-particle events in the MCP from x-ray events and then to veto those events in the HRC electronics. Although the HRC team planned using the HRC anti-co shield and MCP detector total event rates as radiation-monitor inputs, implementation halted during pre-launch software development after incorporation of EPHIN as *Chandra*'s radiation monitor. By design, EPHIN is a more versatile particle counter than the HRC anti-co shield and it has a much larger dynamic range.

HRC A-side and B-side electronics each send anti-co rates and total MCP rates to the OBC: Only data from the active side (now A) are meaningful. Recently, the flight operations team patched flight software to substitute these 4 HRC channels for the 4 EPHIN helium channels in the telemetry. If needed, the flight operations team will patch RADMON to substitute an HRC channel for one of the 3 watched EPHIN channels. Complete failure of EPHIN would require an additional patch so that the RADMON process would ignore the EPHIN hardware failure: Currently, RADMON will activate SCS107 if the OBC does not receive an "alive" signal from EPHIN through the EIO and from the EIO.

3.5.3. EPHIN–HRC-anti-co comparison

In order to determine optimal use of the HRC anti-co shield as a radiation monitor, the science operations and HRC teams conducted a comparative study of available EPHIN and HRC-anti-co data. Although the EPHIN operates throughout each orbit, the HRC high voltage (HV) is always "off" during radiation-zone transit. During the first year of the mission, the HRC HV remained "on" outside the radiation zone. Subsequently, the HRC HV was "on" only in conjunction with HRC observations, so as to maximize the operating life of the PMT. As concern over potential EPHIN degradation grew, we resumed collecting HRC anti-co data at all times outside the radiation zone, but at various reduced HV levels when the HRC was not engaged in a science observation.

Using available data, we compared HRC anti-co rates with rates in the 3 EPHIN channels—P4 (4.3–7.8-MeV proton), P41 (41–53-MeV proton), and E1300 (2.6–6.2-MeV electron)—watched by the RADMON process (§2.2.3). Figure 7 exhibits the scatter plots of raw (OBC ingested) HRC anti-co rates versus P4 spectral intensity (left) and versus P41 spectral intensity (right). The vertical line in each plot demarcates the respective threshold for RADMON to activate SCS107. For all anti-co data in Figure 7, the PMT HV had been set to step 8, its nominal setting for operations. Data collected at lower PMT HV steps exhibits the same behavior as shown in these plots. Not surprisingly, the HRC anti-co data correlates best with data from EPHIN's highest energy proton channel (P41)—i.e., the most penetrating radiation. The correlation with other EPHIN channels becomes progressively worse for less penetrating radiation.

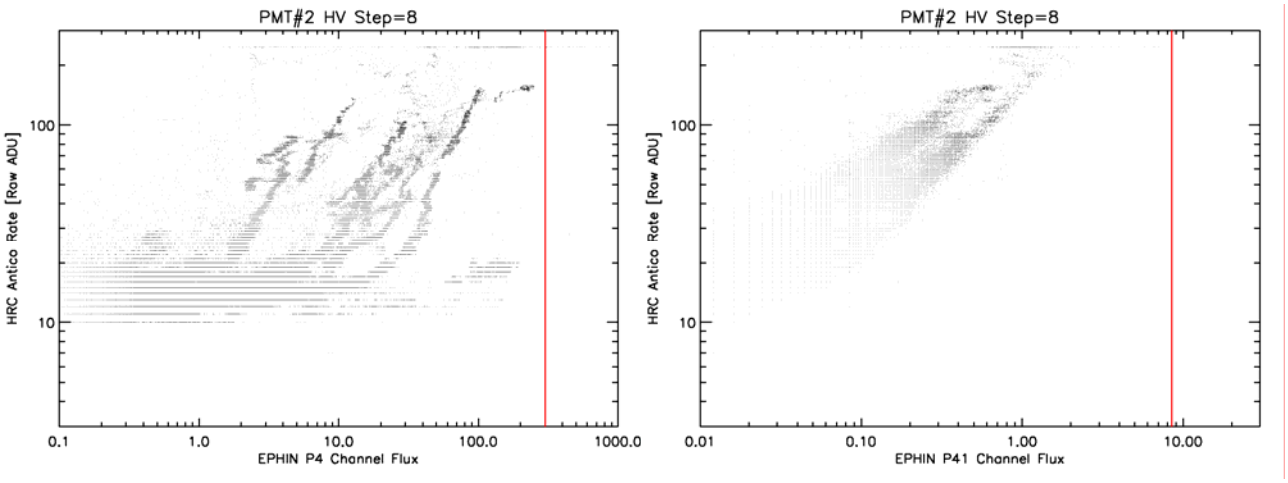

Figure 7: Comparison of raw HRC anti-co rates with proton intensity in EPHIN channels P4 (left) and P41 (right). HRC anti-co rates are in analog–digital units (ADU); EPHIN, #/(cm^2 s sr). The vertical lines are current RADMON thresholds for autonomous activation of radiation protection (SCS107). Note the data-handling ceiling in anti-co rates at 248 ADU.

A potentially important limitation in the HRC anti-co data is a data-handling ceiling at 248 ADU (analog–digital units), set to avoid overflow of the single byte encoding the anti-co rate. Figure 7 clearly evidences this ceiling and that the anti-co rate typically reaches it before any EPHIN channel reaches its respective SCS107 threshold. The RADMON threshold for the HRC anti-co rate—necessarily less than its ceiling—might result in many unnecessary SCS107 activations. However, an investigation of EPHIN-triggered SCS107 and instances for which the anti-co rate would have triggered SCS107 alleviates this concern: Requiring 10 consecutive EPHIN samples above threshold, the anti-co rate would have triggered SCS107 for 6 of 14 EPHIN triggers, but would never have triggered without an EPHIN trigger.

3.5.4. Contingency plans

For *Chandra* radiation protection, HRC anti-co data are a poor substitute for EPHIN data. Whereas weakly penetrating radiation (0.1–0.5-MeV protons) causes most of the damage to the FI CCDs, the anti-co shield is sensitive only to penetrating radiation. Although not ideal, the EPHIN P4 channel (4.3–7.8-MeV proton) is a much better proxy for the lower energy protons of most concern. Further, while the HRC anti-co shield is a reasonably good proxy for the EPHIN P41 channel (§3.5.3), P41 seldom triggers SCS107. Hence, the data-handling ceiling on HRC anti-co rates would probably not result in frequent unnecessary radiation safings. Indeed, the investigation of past SCS107 triggers found that the HRC anti-co rate would not have triggered about half the radiation safings triggered by EPHIN rates. On the

other hand, the HRC anti-co rate would have triggered the other half and certainly would preclude an unprotected perigee pass—by far the most damaging radiation event for the ACIS FI CCDs.

Our strategy then is to employ HRC anti-co data in autonomous radiation protection only when they contribute capability that is no longer available from the EPHIN. Of course, a catastrophic failure of EPHIN will require that we use the HRC anti-co shield as the *Chandra* radiation monitor. However, the expected scenario (§3.5.1) is a "graceful degradation" with the higher energy EPHIN channels—those relying most on the lithium-drifted silicon detectors in the detector stack—becoming noisy first. If fewer than 3 EPHIN channels are useful, RADMON will then watch HRC anti-co rates and the remaining EPHIN channel(s) for autonomous radiation safing. It is some comfort that the EPHIN P4 channel—the most relevant to radiation protection of the ACIS—is the least sensitive to thermal degradation.

REFERENCES

[1] M.C. Weisskopf, T.L. Aldcroft, M. Bautz, R.A. Cameron, D. Dewey, J.J Drake, C.E Grant, H.L. Marshall, & S.S. Murray, "An Overview of the Performance of the Chandra X-ray Observatory", Exp. Astron., **16**, 1–68, 2003.

[2] M.C. Weisskopf, B. Brinkman, C. Canizares, G. Garmire, S. Murray, & L.P. Van Speybroeck, "An Overview of the Performance and Scientific Results from the Chandra X-Ray Observatory", Pub. Astron. Soc. Pacific, **114**, 1–24, 2002.

[3] M.C. Weisskopf, H.D. Tananbaum, L.P. Van Speybroeck, & S.L. O'Dell, "Chandra X-ray Observatory (CXO): overview", Proc. SPIE, **4012**, 2–16, 2000.

[4] S.S. Murray, G.K. Austin, J.H. Chappell, J.J. Gomes, A.T. Kenter, R.P. Kraft, G.R. Meehan, M.V. Zombeck, G.W. Fraser, & S. Serio, "In-flight performance of the Chandra High-Resolution Camera", Proc. SPIE, **4012**, 68–80, 2000.

[5] G.P. Garmire, M.W. Bautz, P.G. Ford, J.A. Nousek, & G.R. Ricker Jr., "Advanced CCD Imaging Spectrometer (ACIS) instrument on the Chandra X-ray Observatory", Proc. SPIE, **4851**, 28–44, 2003.

[6] G.Y. Prigozhin, S.E. Kissel, M.W. Bautz, C.E. Grant, B. LaMarr, R.F. Foster, & G.R. Ricker, "Radiation damage in the Chandra x-ray CCDs", Proc. SPIE, **4012**, 720–730, 2000.

[7] G.Y. Prigozhin, S.E. Kissel, M.W. Bautz, C.E. Grant, B. LaMarr, R.F. Foster, & G.R. Ricker, "Characterization of the radiation damage in the Chandra x-ray CCDs", Proc. SPIE, **4140**, 123–134, 2000.

[8] S.L. O'Dell, M.W. Bautz, W.C. Blackwell Jr., Y.M Butt, R.A. Cameron, R.F. Elsner, M.S. Gussenhoven, J.J. Kolodziejczak, J.I. Minow, R.M. Suggs, D.A. Swartz, A.F. Tennant, S.N. Virani, & K.M. Warren, "Radiation environment of the Chandra X-Ray Observatory", Proc. SPIE, **4140**, 99–110, 2000.

[9] J.J. Kolodziejczak, R.F. Elsner, R.A. Austin, & S.L. O'Dell, "Ion transmission to the focal plane of the Chandra X-ray Observatory", Proc. SPIE, **4140**, 135–143, 2000.

[10] S.L. O'Dell, W.C. Blackwell Jr., R.A. Cameron, J.I. Minow, D.C. Morris, B.J Spitzbart, D.A. Swartz, S.N. Virani, & S.J. Wolk, "Managing radiation degradation of CCDs on the Chandra X-ray Observatory", Proc. SPIE, **4851**, 77–88, 2003. (Paper I)

[11] `http://www.spenvis.oma.be/spenvis/`

[12] E.C. Stone, A.M. Frandsen, R.A. Mewaldt, E.R. Christian, D. Margolies, J.F. Ormes, & F. Snow, "The Advanced Composition Explorer", Space Science Rev., **86**, 1–22, 1998.

[13] E.C. Stone, C.M.S. Cohen, W.R. Cook, A.C. Cummings, B. Gauld, B. Kecman, R.A. Leske, R.A. Mewaldt, M.R. Thayer, B.L. Dougherty, R.I. Grumm, B.D. Milliken, R.G. Radocinski, M.E. Wiedenbeck, E.R. Christian, S. Shuman, & T.T. von Rosenvinge, "The Solar Isotope Spectrometer for the Advanced Composition Explorer", Space Science Rev., **86**, 357–408, 1998.

[14] R.E. Gold, S.M. Krimigis, S.E. Hawkins III, D.K. Haggerty, D.A. Lohr, E. Fiore, T.P. Armstrong, G. Holland, & L.J. Lanzerotti, "Electron, Proton and Alpha Monitor on the Advanced Composition Explorer spacecraft", Space Science Rev., **86**, 541–562, 1998.

[15] W.C. Blackwell Jr., J.I. Minow, K .Warren, R.M. Suggs, S.L. O'Dell, D.A. Swartz, A.F. Tennant, & S.N. Virani, "Modeling the Chandra space environment", Proc. SPIE, **4140**, 111–122, 2000.

[16] R. Müller-Mellin, H. Kunow, V. Fleissner, E. Pehlke, E. Rode, N. Roschmann, C. Scharmberg, H. Sierks, P. Rusznyak, I.E.S. McKenna-Lawlor, J. Sequeiros, D. Meziat, S. Sanchez, J. Medina, L. der Peral, M. Witte, R. Marsden, & J. Henrion, "COSTEP—comprehensive suprathermal and energetic particle analyzer", Solar Phys., **162**, 483–504, 1995.

[17] C.E. Grant, M.W. Bautz, S.E. Kissel, B.W. LaMarr, & G.Y. Prigozhin, "Long-term trends in radiation damage of Chandra x-ray CCDs", Proc. SPIE, **5898**, [Paper 27], 2005.

[18] C.E. Grant, G.Y. Prigozhin, B. LaMarr, & M.W. Bautz, "Sacrificial charge and the spectral resolution performance of the Chandra advanced CCD imaging spectrometer", Proc. SPIE, **4851**, 140–148, 2003.

[19] C.E. Grant, M.W. Bautz, S.E. Kissel, & B. LaMarr, "A charge transfer inefficiency correction model for the Chandra advanced CCD imaging spectrometer", Proc. SPIE, **5501**, 177–188, 2004.

[20] L.K. Townsley, P.S. Broos, J.A Nousek, & G.P. Garmire, G. P., "Modeling charge transfer inefficiency in the Chandra Advanced CCD Imaging Spectrometer", Nucl. Instruments Methods Phys. Res. A, **486**, 751–784, 2002.

[21] P.P. Plucinsky, N.S. Schulz, H.L. Marshall, C.E. Grant, G. Chartas, D. Sanwal, M. Teter, A.A. Vikhlinin, R.J. Edgar, M.W. Wise, G.E. Allen, S.N. Virani, J.M. DePasquale, & M.T. Raley, "Flight spectral response of the ACIS instrument", Proc. SPIE, **4851**, 89–100, 2003.

[22] S.N. Virani, R. Müller-Mellin, P.P. Plucinsky, & Y.M. Butt, "Chandra X-ray Observatory's radiation environment and the AP-8/AE-8 model", Proc. SPIE, **4012**, 669–680, 2000.

[23] S.N. Virani, J.M. DePasquale, D.A. Schwartz, R.A. Cameron, P.P. Plucinsky, S.L. O'Dell, J.I. Minow, & W.C. Blackwell Jr., "Improving the science observing efficiency of the Chandra X-ray Observatory via the Chandra radiation model", Proc. SPIE, **5165**, 530-541, 2004.

[24] J.M. DePasquale, S.N. Virani, D.A. Schwartz, R.A. Cameron, P.P. Plucinsky, S.L. O'Dell, J.I. Minow, W.C. Blackwell Jr., "A study of the seasonal variations of the Chandra X-ray Observatory radiation model", Proc. SPIE, **5165**, 554-564, 2004.

[25] G.E. Villa, A.F. Abbey, M. Arnaud, M. Balasini, G.F. Bignami, M. Boer, H. Brauninger, I. Butler, G. Cafagna, C. Cara, C. Chabaud, L. Chiappetti, R.E. Cole, M. Conte, J. Dowson, P. Dhez, R. Duc, G. di Cocco, P. Ferrando, C.V. Goodall, H. Hippman, A.D. Holland, E. Kendziorra, A. Labeque, N. Meidinger, C. Moriggio, N. La Palombara, C. Musso, E. Poindron, G. Peres, E. Pferreman, C. Pigot, J.P. Pye, C. Reppin, D. Schmitt, S. Sciortino, S. Serio, J. Spragg, J.B. Stephen, L. Struder, M. Trifoglio, P. Tua, M.J. Turner, S. Whitehead, "EPIC system onboard the ESA XMM", Proc. SPIE, **2808**, 402–413, 1996.

[26] D.J. Williams, R.W. McEntire, C. Schlemm II, A.T.Y. Lui, G. Gloeckler, S.P. Christon, & F. Gliem, "Geotail Energetic Particles and Ion Composition instrument", J. Geomag. Geoelect., **46**, 39–57, 1994.

[27] H. Spence & J. Blake, "First observations by the CEPPAD imaging proton spectrometer aboard Polar", Advances in Space Res., **20**, 933–936, 1998.

[28] D.J. McComas, S.J. Bame, P. Barker, W.C. Feldman, J.L. Phillips, P. Riley, & J.W. Griffee, "Solar-Wind Electron Proton Alpha Monitor (SWEPAM) for the Advanced Composition Explorer", Space Science Rev., **86**, 563–612, 1998.

[29] R.D. Zwickl, K.A. Doggett, S. Sahm, W.P. Barrett, R.N. Grubb, T.R. Detman, V.J. Raben, C.W. Smith, P. Riley, R.E. Gold, R.A. Mewaldt, & S. Maruyama, "The NOAA Real-Time Solar-Wind (RTSW) system using ACE data", Space Science Rev., **86**, 633–648, 1998.

[30] K.A. Costello, "Moving the Rice MSFM into real-time forecast mode using solar-wind driven forecast models", Ph. D. dissertation, Rice University, June 1997.

[31] J.B. Blake, D.N. Baker, N. Turner, K.W. Ogilvie, & R.P. Lepping, "Correlation of changes in the outer-zone relativistic-electron population with upstream solar-wind and magnetic-field measurements", Geophys. Res. Lett., **24**, 927–930, 1997.

[32] D.N. Baker, S.G. Kanekal, J.B. Blake, & T.I. Pulkkinen, "The global efficiency of relativistic-electron production in the Earth's magnetosphere", J. Geophys. Res., **106**, 19169–19178, 2001.

[33] X. Li, D.N. Baker, S.G. Kanekal, M. Looper, & M. Temerin, "Long-term measurements of radiation belts by SAMPEX and their variations", Geophys. Res. Lett., **28**, 3827–3830, 2001.